中國機械工程學刊第四十四卷第一期第 91~98 頁(民國一百一十二年)
Journal of the Chinese Society of Mechanical Engineers, Vol.44, No.1, pp 91~98 (2023)

Inverse Dynamics in the Joint Space of a Redundantly Actuated Parallel Mechanism Constrained by Two Point-Contact Higher Kinematic Pairs

Chen Cheng*, Xiaojing Yuan**, Fanqi Zeng*, Weipeng Luo* and Ze Zhang*

Keywords: Inverse dynamics, Higher kinematic pair, Spatial parallel mechanism, Redundant actuation, Joint space.

ABSTRACT

This paper presents the rigid-body inverse dynamics of a spatial redundantly actuated parallel mechanism (RAPM) constrained by two point-contact higher kinematic pairs (HKPs). Firstly, its constrained motions are analysed comprehensively, Then the dynamic model is built by the decoupled natural orthogonal complement (DeNOC) in the joint space, which is very suitable for the model-based motion control. The influences by HKPs in the model structure, the computational time, and the torque cost are discovered clearly. The NOC matrix is decoupled into three matrices, which is very different from those in PMs without actuation redundancy. The comparisons between the RAPM and its counterpart free of HKPs clearly validate that the constraints at HKPs considerably increase the computational cost, and the torques required by the parasitic motions of the end effector are significantly smaller than those by the corresponding DOFs.

INTRODUCTION

In the food industry, there is a strong interest in evaluating the time-varying dynamics of newly developed food textures during the chewing process. To this end, a machine that can accurately replicate the human-like chewing behaviours such as the three-dimensional (3D) chewing motions and bite forces in a biomimetic fashion can come into play a significant role. Inspired by the masticatory system of human beings, a spatial parallel mechanism (PM) constrained by two point-contact higher kinematic pairs (HKPs) has been developed (Cheng, Xu, and Shang 2015): the base is the skull, the six <u>R</u>SS (revolute-spherical-spherical) kinematic chains are the primary chewing muscles, the end effector is the mandible, and the two HKPs are the left and right temporomandibular joints (TMJs), respectively. The underlined letter means the joint is active in the chain. From the viewpoint of mechanism, the masticatory system is redundantly actuated, for it owns more chewing muscles than its degrees of freedom (DOFs). Meanwhile, during its movements, the lower jaw is always constrained by the maxilla at two TMJs. In the designed PM, the number of actuations is also larger than that of the DOFs, and the end effector is directly constrained by the base at two HKPs. Therefore, these two features are in a good agreement with the human masticatory system, and it is a biologically congruent redundantly actuated parallel mechanism (RAPM) constrained at HKPs. Readers interested in the human masticatory system and chewing robotics can refer to (Xu and Bronlund 2010) for a comprehensive description.

Compared to serial mechanisms, PMs have better payload capacities, larger stiffness, and higher motion accuracy (Merlet 2012). Actuation redundancy can better enhance these advantages (Muller 2005). To realise them in practice, a suitable inverse dynamic model that can contribute to the model-based motion and/or force control is needed. Due to the nature of actuation redundancy in PMs, actuations in the joint space are not independent. Thus, the inverse dynamics models of RAPMs are usually in the task space, for instance, see (Liu et al. 2022) (Wang et al. 2019) (Shang and Cong 2014) (Cheng, Yiu, and Li 2003). To implement the dynamic model-based motion control,

Paper Received September, 2022. Revised December, 2022. Accepted December, 2022.Author for Correspondence: Chen Cheng

* *Lecturer, Lab of Mechatronics, Xi'an College of Technology, Xi'an, 710024, China.*

** *Professor, Lab of Mechatronics, Xi'an College of Technology, Xi'an, 710024, China.*

the motions in the task space are either measured by exteroceptive optical devices in practice (Bellakehal et al. 2011), or computed by forward kinematics in real-time theoretically (Shang and Cong 2014) (Cheng, Yiu, and Li 2003). However, these two methods pose evident challenges: the exteroceptive devices no doubt increase the hardware cost and complexity. On the other hand, even though in some planar RAPMs forward dynamics is available in a relatively simple manner as in (Cheng, Yiu, and Li 2003) (Liang et al. 2015), however, for the RAPM under study, its forward dynamics is very sophisticated, rendering the computation hardly be realised in real-time. In comparison, a dynamic model in the joint space is easy-to-use and the economic cost is acceptable. The displacements and velocities can be measured by encoders of actuators directly, and accelerations can be computed in a simple manner, then neither exteroceptive devices nor forward kinematics is needed. More importantly, the great number of advanced control schemes developed for serial manipulators in the joint space can be easily extended to this RAPM. In these regards, building an inverse dynamics model in its joint space of the RAPM under study is the strong motivation in this paper.

From the literature, the decoupled natural orthogonal complement (DeNOC) (Saha 1999) has attracted our attention. It is developed from the concept of NOC matrix which is explicitly decoupled as a product of a block lower triangular matrix and a block diagonal matrix. This method has some advantages such as many physical interpretations of the vectors and matrices, and recursive inverse/forward dynamics algorithms (Rao, Saha, and Rao 2006). Due to these, it has been employed widely in various mechanisms recently. For instance, it was used to the inverse and forward dynamics of serial-chain manipulators (Saha 1999), and the inverse dynamics of both planar (Khan et al. 2005) and spatial (Rao, Saha, and Rao 2006) PMs. The virtual spring method was incorporated into it to resolve the forward dynamics of a planar $\underline{R}$RRR$\underline{R}$ PM with two DOFs (Raoofian, Kamali, and Taghvaeipour 2017). In (Rahmani Hanzaki, Saha, and Rao 2009), this method was combined with Euler parameters to build improved rigid body dynamic models of multibody systems with spherical joints. It was further utilised to build the model of a planar compliant robotic fish in (Jiang and Liu 2021).

In this paper, an attempt has been made to adopt the DeNOC to build the dynamics model of the RAPM, and it is believed the first to apply this method to a RAPM constrained by the base directly. In the dynamics modelling, it is assumed that all bodies and joints are rigid and free of clearances or friction. The inertia of the spherical joints is rather small and ignored. A detailed description of the mechanism is presented first, then the kinematics including the constrained end effector and the chains is analysed comprehensively. On this basis, the inverse dynamics of the RAPM in its joint space is formatted by the DeNOC. The numerical computations and the influences of the constraints at HKPs in the inverse dynamics are presented. Some conclusions are drawn in the end.

THE MECHANISM

The kinematic diagram of the PM constrained by the base at two HKPs is illustrated in Figure. 1(a). The maxilla (i.e., the base) is fixed on the ground and the movable mandible (i.e., the end effector) is driven by six independent kinematic chains. For a clear exhibition of movable bodies, the main part of the maxilla is not shown in the figure. However, the articular surfaces of TMJs belonging to the maxilla are exhibited to show the point-contact HKPs.

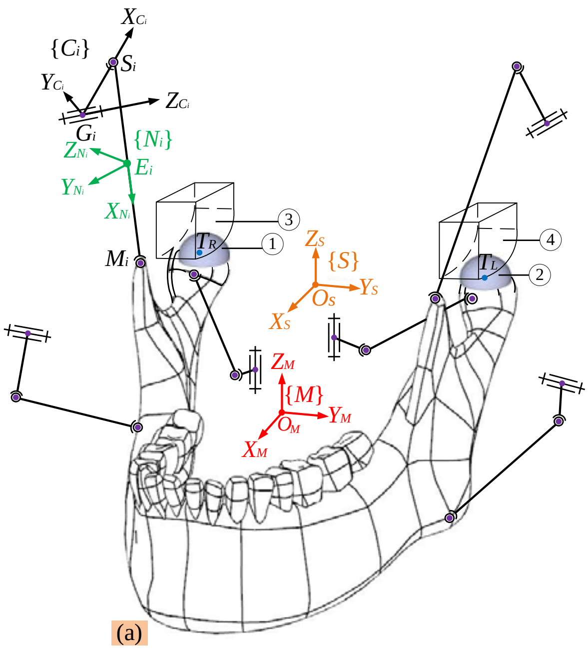

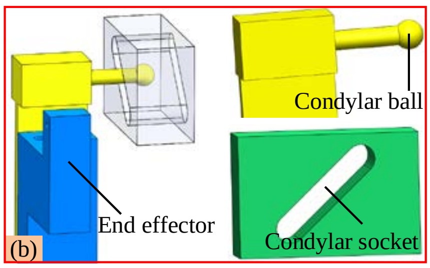

Fig. 1 The constrained PM by the base at two point-contact HKPs, (a). Its schematic diagram where ① ② are condyle balls, and ③ ④ are articular surfaces of TMJs (Cheng, Xu, and Shang 2015), (b). A point-contact HKP and related mechanical parts.

The inertia frame $\{S\}$ attached to the maxilla consists of a horizontal X_S-Y_S plane perpendicular to the vertical Z_S axis. A frame $\{M\}$ is established at the mass centre O_M of the end effector. The origins and orientations of {S} and {M} overlap when the mechanism is at the home position, that is, the maxilla and the mandible are in the occlusal state. The origin O_M is used as the reference point to describe the mandibular translations, and its orientations with respect to {S} are described by XYZ Euler angles, that is, α , β , and γ around the three axes of {M}. Two point-contact HKPs are formed between the condylar balls ① ② in the lower jaw and the articular surfaces of TMJs ③ ④ at the upper jaw. Each chain contains a rotational actuator fixed onto the base, whose driving shaft connects a crank $\boldsymbol{G_iS_i}$ (i=1,…,6) with a rotational joint at G_i, and a coupler $\boldsymbol{S_iM_i}$ that joins the crank and the end effector via two spherical joints at its two ends S_i and M_i, respectively. The rotation of the ith actuator with respect to {S} is described by the actuator frame $\{C_i\}$ attached at G_i. In it, the X_{C_i} axis is directed from G_i to S_i, the Z_{C_i} axis runs through the driving shaft of the actuator, and the Y_{C_i} axis completes the frame, obeying the right-hand rule. A frame {N_i} is attached at the mass centre E_i of $\boldsymbol{S_iM_i}$ to describe its motions with respect to {S}. The X_{N_i} axis points from S_i to M_i, the Y_{N_i} axis is parallel to the cross product of two unit vectors defined along the X_{N_i} and X_S axes, and the Z_{N_i} axis is defined by the right-hand rule. From **Fig. 1(a)**, the end effector is driven by six chains and constrained by the base at two HKPs simultaneously.

A point-contact HKP and its related mechanical parts in **Fig. 1(b)** show the practical mechanical design of HKPs. The condylar ball slips along a condylar socket with a width equal to the diameter of the ball. Thus, the point-contact HKP during the movements of the end effector is always guaranteed.

KINEMATICS OF THE MECHANISM

The constrained end effector

A second-order surface was used as the workspace of the centre of the condylar ball in (Cheng, Xu, and Shang 2015). However, it is very difficult to derive explicit analytical expressions of the parasitic motions under the second-order surface when the frame {M} is situated at the mass centre of the end effector. Regarding it, in this paper where the chewing system is explored from the viewpoint of constrained mechanical dynamics, the surfaces in {S} where the left and right condyle ball centres T_i (i=L, R) slide on are designed as flat (unit: mm)

$$\boldsymbol{O}_S\boldsymbol{T}_i = \begin{bmatrix} X_i \\ Y_i \\ Z_i \end{bmatrix}, \quad \begin{array}{l} Z_i = p_1 X_i + p_2, \quad p_3 \le X_i \le p_4 \\ p_5 \le Y_L \le p_6, \quad -p_6 \le Y_R \le -p_5 \\ p_1 = -1.1,\ p_2 = 13.215,\ p_3 = -27.65 \\ p_4 = -14.65,\ p_5 = 69,\ p_6 = 75 \end{array} \tag{1}$$

where p_1 is a dimensionless parameter, while the unit of p_2~ p_6 is millimetre.

From the Kutzbach-Grübler criterion, the mechanism has four DOFs, but the information on which four to choose is not given. They are to be derived from a rigorous computation below.

The coordinates of T_i (i=L,R) in {S} can be expressed as

$$\boldsymbol{O}_S\boldsymbol{T}_i = \boldsymbol{O}_S\boldsymbol{O}_M + {}^S_M\boldsymbol{R} \cdot {}^M\boldsymbol{O}_M\boldsymbol{T}_i \tag{2}$$

where $\boldsymbol{O}_S\boldsymbol{O}_M = \begin{bmatrix} X & Y & Z \end{bmatrix}^T$ denotes the 3×1 position vector of O_M in {S}, ${}^S_M\boldsymbol{R} = \boldsymbol{R}_X(\alpha)\cdot\boldsymbol{R}_Y(\beta)\cdot\boldsymbol{R}_Z(\gamma)$ is the rotation matrix from {S} to {M}, $\boldsymbol{R}_X(\alpha)$, $\boldsymbol{R}_Y(\beta)$, and $\boldsymbol{R}_Z(\gamma)$ are three rotation matrices about the X_M, Y_M, and Z_M axes by three Bryant angles α , β , and γ , respectively, and ${}^M\boldsymbol{O}_M\boldsymbol{T}_i$ is the vector $\boldsymbol{O}_M\boldsymbol{T}_i$ in {M}. It is worth noting that in this paper, a position vector in a local frame owns a leading superscript on its left to denote the specific frame it refers to, but those in {S} omit the superscript for the sake of clarity.

From Eq. (2), one can obtain

$$\begin{aligned} X_i &= X + {}^S_M\boldsymbol{R}_{(1,:)} \cdot {}^M\boldsymbol{O}_M\boldsymbol{T}_i \\ Z_i &= Z + {}^S_M\boldsymbol{R}_{(3,:)} \cdot {}^M\boldsymbol{O}_M\boldsymbol{T}_i \end{aligned} \tag{3}$$

where ${}^S_M\boldsymbol{R}_{(j,:)}$ is the jth(j=1,3) row of ${}^S_M\boldsymbol{R}$. Putting Eq. (3) into Eq. (1) produces

$$Z + {}^S_M\boldsymbol{R}_{(3,:)} \cdot {}^M\boldsymbol{O}_M\boldsymbol{T}_i = p_1 \cdot \left(X + {}^S_M\boldsymbol{R}_{(1,:)} \cdot {}^M\boldsymbol{O}_M\boldsymbol{T}_i \right) + p_2 \tag{4}$$

Because of the left-right symmetry of ${}^M\boldsymbol{O}_M\boldsymbol{T}_L$ and ${}^M\boldsymbol{O}_M\boldsymbol{T}_R$ in {M}, a summation and a subtraction of the two equations in Eq. (4) yield

$$Z = p_1 X + p_2 + \left(p_1 \cdot {}^S_M\boldsymbol{R}_{(1,:)} - {}^S_M\boldsymbol{R}_{(3,:)} \right) \cdot \begin{bmatrix} {}^M\boldsymbol{O}_M\boldsymbol{T}_{L(1)} \\ 0 \\ {}^M\boldsymbol{O}_M\boldsymbol{T}_{L(3)} \end{bmatrix} \tag{5}$$

$$\gamma = -\mathrm{a}\tan \frac{s\alpha}{p_1 \mathrm{c}\beta + c\alpha s\beta}$$

where ${}^M\boldsymbol{O}_M\boldsymbol{T}_{L(j)}\ (j=1,3)$ are the jth term of ${}^M\boldsymbol{O}_M\boldsymbol{T}_L$. From these computations, Z and γ are transferred from DOFs to parasitic motions and they are functions of $\boldsymbol{q}_{EE}$, which is a 4◊ 1vector by grouping four DOFs as

$$\boldsymbol{q}_{EE} = \begin{bmatrix} X & Y & \alpha & \beta \end{bmatrix}^T \tag{6}$$

and it constitutes the task space of the RAPM.

In this case, to characterise the instantaneous configuration of the mechanism, both Eqs. (5) and (6) are needed. In other words, the RAPM can still perform motions in six directions with four DOFs and two parasitic motion variables. Regarding this, redundant actuations in the mechanism are essentially caused by constraints from the base directly onto the end effector, converting two DOFs into parasitic motion variables. This is completely different from the two methodologies mentioned in (Gosselin and Schreiber 2018), namely, adding identical chains as those existing in the PM, or actuating passive joints in the chain. It is also worth noting that though the workspace of the centre of the condylar ball is simplified as a flat surface as in Eq. (1), a strongly nonlinear and sophisticated relationship between Z/γ and $\boldsymbol{q}_{EE}$ in Eq. (6) can still be observed.

The *i*th chain

The inverse kinematics of the RAPM, i.e., $\boldsymbol{\theta}=\boldsymbol{\theta}(\boldsymbol{q}_{EE})\left(\boldsymbol{\theta}=[\theta_1 \ \cdots \ \theta_6]^T\right)$ that consists of a system of six decoupled equations expressed by $\boldsymbol{q}_{EE}$, has already been derived in Section II of (Cheng, Xu, and Shang 2015). Nevertheless, the motions of the coupler $\boldsymbol{S}_i\boldsymbol{M}_i$($i$=1,…,6) are still needed for the rigid-body dynamics of the RAPM. Due to the two spherical joints at $\boldsymbol{S}_i$ and $\boldsymbol{M}_i$, the coupler can rotate around the three orthogonal axes of $\{N_i\}$. However, the rotation around the X_{N_i} axis is a passive DOF for it is not controllable, and this rotational range is very small thanks to the physical restrictions from the used spherical joints in the mechanical design. In these regards, it is assumed that there is no axial rotation in the coupler. As such, two Euler angles β_i and γ_i around the Y_{N_i} and Z_{N_i} axes, respectively, are used to express the rotation of $\boldsymbol{S}_i\boldsymbol{M}_i$ in $\{S\}$. These two angles can be derived as functions of the DOFs of the end effector, which is very well-established as in (Cheng, Yiu, and Li 2003) (Huang, Chen, and Zhong 2013). Thereby, the details are not listed. A 3◊ 1 generalised vector defined as $\boldsymbol{q}_{r_i}=[\theta_i \ \ \beta_i \ \ \gamma_i]^T$ consists of the space of the ith chain and is used to completely specify its configuration. Then $\boldsymbol{q}_{r_i}$ is the function of $\boldsymbol{q}_{EE}$, namely, $\boldsymbol{q}_{r_i}=\boldsymbol{q}_{r_i}(\boldsymbol{q}_{EE})$. Moreover, one can find that

$$\dot{\boldsymbol{q}}_{r_i}=\boldsymbol{M}_{1i}\cdot\dot{\boldsymbol{q}}_{EE} \tag{7}$$

from which $\dot{\theta}_i$ can be extracted as

$$\dot{\theta}_i=\boldsymbol{M}_{1i(1,:)}\cdot\dot{\boldsymbol{q}}_{EE} \tag{8}$$

where $\boldsymbol{M}_{1i(1,:)}\,(i=1,...,6)$ is the first line of $\boldsymbol{M}_{1i}$.

For the crank $\boldsymbol{G}_i\boldsymbol{S}_i$, it only rotates with respect to the Z_{C_i} axis of frame $\{C_i\}$, then its angular velocity is

$$\boldsymbol{\omega}_{\boldsymbol{G}_i\boldsymbol{S}_i}={}_{C_{i0}}^{S}\boldsymbol{R}\cdot\boldsymbol{R}_Z(\theta_i)\cdot\begin{bmatrix}\boldsymbol{0}_{2\times1}\\ \dot{\theta}_i\end{bmatrix}={}_{C_{i0}}^{S}\boldsymbol{R}_{(:,3)}\cdot\dot{\theta}_i \tag{9}$$

in which ${}_{C_{i0}}^{S}\boldsymbol{R}$ is the orientation of $\{C_i\}$ in $\{S\}$ at the initial configuration of the RAPM, $\boldsymbol{R}_Z(\theta_i)$ is the rotation matrix about the Z_{C_i} axis by θ_i, and ${}_{C_{i0}}^{S}\boldsymbol{R}_{(:,3)}$ is the third column of ${}_{C_{i0}}^{S}\boldsymbol{R}$.

The mass centre G_i of the crank is fixed in $\{S\}$, thus $\boldsymbol{V}_{G_i}=\boldsymbol{0}_{3\times1}$. As a result, the twist of the crank $\boldsymbol{G}_i\boldsymbol{S}_i$ is

$$\boldsymbol{t}_{\boldsymbol{G}_i\boldsymbol{S}_i}=\begin{bmatrix}\boldsymbol{\omega}_{\boldsymbol{G}_i\boldsymbol{S}_i}\\ \boldsymbol{V}_{G_i}\end{bmatrix}=\boldsymbol{M}_{1\boldsymbol{G}_i\boldsymbol{S}_i}\cdot\dot{\theta}_i \tag{10}$$

where $\boldsymbol{M}_{1\boldsymbol{G}_i\boldsymbol{S}_i}=\begin{bmatrix}{}_{C_{i0}}^{S}\boldsymbol{R}_{(:,3)}\\ \boldsymbol{0}_{3\times1}\end{bmatrix}$. On this basis, the linear velocity of S_i is computed as

$$\boldsymbol{V}_{S_i}=\boldsymbol{M}_{2\boldsymbol{G}_i\boldsymbol{S}_i}\cdot\boldsymbol{M}_{1\boldsymbol{G}_i\boldsymbol{S}_i}\cdot\dot{\theta}_i \tag{11}$$

where $\boldsymbol{M}_{2\boldsymbol{G}_i\boldsymbol{S}_i}=[-\boldsymbol{G}_i\boldsymbol{S}_i\times \ \ \boldsymbol{E}_3]$.

The linear velocity of M_i is computed as

$$\boldsymbol{V}_{M_i}=\boldsymbol{A}_{EE_i}\cdot\boldsymbol{t}_{EE} \tag{12}$$

where $\boldsymbol{A}_{EE_i}=[-\boldsymbol{O}_M\boldsymbol{M}_i\times \ \ \boldsymbol{E}_3]$ and $\boldsymbol{t}_{EE}$ is the twist of the end effector. Thereby, the linear velocity of the mass centre E_i of the coupler $\boldsymbol{S}_i\boldsymbol{M}_i$ is

$$\begin{aligned}\boldsymbol{V}_{E_i}&=\frac{1}{2}\cdot\left(\boldsymbol{V}_{M_i}+\boldsymbol{V}_{S_i}\right)\\&=\frac{1}{2}\cdot\boldsymbol{A}_{EE_i}\cdot\boldsymbol{t}_{EE}+\frac{1}{2}\cdot\boldsymbol{M}_{2\boldsymbol{G}_i\boldsymbol{S}_i}\cdot\boldsymbol{M}_{1\boldsymbol{G}_i\boldsymbol{S}_i}\cdot\dot{\theta}_i\end{aligned} \tag{13}$$

From the assumption made about the rotation of the coupler $\boldsymbol{S}_i\boldsymbol{M}_i$, its angular velocity is perpendicular to the X_{N_i} axis of $\{N_i\}$, thus

$$\boldsymbol{\omega}_{\boldsymbol{S}_i\boldsymbol{M}_i}=\boldsymbol{B}_{\boldsymbol{S}_i\boldsymbol{M}_i}\cdot\left(\boldsymbol{V}_{M_i}-\boldsymbol{V}_{S_i}\right) \tag{14}$$

where $\boldsymbol{B}_{\boldsymbol{S}_i\boldsymbol{M}_i}=\dfrac{\boldsymbol{S}_i\boldsymbol{M}_i\times}{\left\|\boldsymbol{S}_i\boldsymbol{M}_i\right\|^2}$. In it, $\boldsymbol{S}_i\boldsymbol{M}_i\times$ and $\left\|\boldsymbol{S}_i\boldsymbol{M}_i\right\|$ are the skew matrix and the length of $\boldsymbol{S}_i\boldsymbol{M}_i$, respectively.

Upon substitution of Eqs. (11) and (12) into Eq. (14), it produces

$$\boldsymbol{\omega}_{\boldsymbol{S}_i\boldsymbol{M}_i}=\boldsymbol{B}_{\boldsymbol{S}_i\boldsymbol{M}_i}\cdot\boldsymbol{A}_{EE_i}\cdot\boldsymbol{t}_{EE}-\boldsymbol{B}_{\boldsymbol{S}_i\boldsymbol{M}_i}\cdot\boldsymbol{M}_{2\boldsymbol{G}_i\boldsymbol{S}_i}\cdot\boldsymbol{M}_{1\boldsymbol{G}_i\boldsymbol{S}_i}\cdot\dot{\theta}_i \tag{15}$$

In view of Eqs. (13) and (15), the twist of the coupler $\boldsymbol{S}_i\boldsymbol{M}_i$ is

$$\boldsymbol{t}_{\boldsymbol{S}_i\boldsymbol{M}_i}=\begin{bmatrix}\boldsymbol{\omega}_{\boldsymbol{S}_i\boldsymbol{M}_i}\\ \boldsymbol{V}_{E_i}\end{bmatrix}=\boldsymbol{C}_{EE_i}\cdot\boldsymbol{t}_{EE}+\boldsymbol{D}_{EE_i}\cdot\boldsymbol{M}_{1\boldsymbol{G}_i\boldsymbol{S}_i}\cdot\dot{\theta}_i \tag{16}$$

where

$$\boldsymbol{C}_{EE_i}=\begin{bmatrix}\boldsymbol{B}_{\boldsymbol{S}_i\boldsymbol{M}_i}\\ 0.5\cdot\boldsymbol{E}_3\end{bmatrix}\cdot\boldsymbol{A}_{EE_i},\quad \boldsymbol{D}_{EE_i}=\begin{bmatrix}-\boldsymbol{B}_{\boldsymbol{S}_i\boldsymbol{M}_i}\\ 0.5\cdot\boldsymbol{E}_3\end{bmatrix}\cdot\boldsymbol{M}_{2\boldsymbol{G}_i\boldsymbol{S}_i}$$

Concerning the rigid-body assumption of the coupler $\boldsymbol{S}_i\boldsymbol{M}_i$, the projections of the two velocities $\boldsymbol{V}_{S_i}$ and $\boldsymbol{V}_{M_i}$ along $\boldsymbol{S}_i\boldsymbol{M}_i$ are equivalent, namely

$$\boldsymbol{S}_i\boldsymbol{M}_i^T\cdot\boldsymbol{V}_{S_i}=\boldsymbol{S}_i\boldsymbol{M}_i^T\cdot\boldsymbol{V}_{M_i} \tag{17}$$

Putting Eqs. (11) and (12) into it yields

$$\boldsymbol{S}_i\boldsymbol{M}_i^T\cdot\boldsymbol{M}_{2\boldsymbol{G}_i\boldsymbol{S}_i}\cdot\boldsymbol{M}_{1\boldsymbol{G}_i\boldsymbol{S}_i}\cdot\dot{\theta}_i=\boldsymbol{S}_i\boldsymbol{M}_i^T\cdot\boldsymbol{A}_{EE_i}\cdot\boldsymbol{t}_{EE} \tag{18}$$

Thereby, for the six actuators, the relationship between $\dot{\boldsymbol{\theta}}$ and $\boldsymbol{t}_{EE}$ is derived as

$$\boldsymbol{Q}_{GS}\cdot\boldsymbol{T}_d\cdot\dot{\boldsymbol{\theta}}=\boldsymbol{J}_{EE}\cdot\boldsymbol{t}_{EE} \tag{19}$$

where

$$\boldsymbol{Q}_{GS} = \mathrm{diag}\left(\boldsymbol{S}_1\boldsymbol{M}_1^{\ T}\cdot\boldsymbol{M}_{2\boldsymbol{G}_1\boldsymbol{S}_1} \quad \cdots \quad \boldsymbol{S}_6\boldsymbol{M}_6^{\ T}\cdot\boldsymbol{M}_{2\boldsymbol{G}_6\boldsymbol{S}_6}\right)$$

$$\boldsymbol{T}_d = \mathrm{diag}\left(\boldsymbol{M}_{1\boldsymbol{G}_1\boldsymbol{S}_1} \quad \cdots \quad \boldsymbol{M}_{1\boldsymbol{G}_6\boldsymbol{S}_6}\right)$$

$$\boldsymbol{J}_{EE} = \begin{bmatrix} \boldsymbol{S}_1\boldsymbol{M}_1^{\ T}\cdot\boldsymbol{A}_{EE_1} \\ \vdots \\ \boldsymbol{S}_6\boldsymbol{M}_6^{\ T}\cdot\boldsymbol{A}_{EE_6} \end{bmatrix}$$

and $\boldsymbol{T}_d$ is a constant block diagonal matrix under Eq. (10).

As a result, the twist of the end effector can be expressed by the active joint rates as

$$\boldsymbol{t}_{EE} = \boldsymbol{J}_{EE}^{-1}\cdot\boldsymbol{Q}_{GS}\cdot\boldsymbol{T}_d\cdot\dot{\boldsymbol{\theta}} \tag{20}$$

when $\boldsymbol{J}_{EE}$ is not singular.

DYNAMICS MODELLING

From Eqs. (10) and (16), the twist of the ith chain is

$$\boldsymbol{t}_{C_i} = \begin{bmatrix} \boldsymbol{t}_{\boldsymbol{G}_i\boldsymbol{S}_i} \\ \boldsymbol{t}_{\boldsymbol{S}_i\boldsymbol{M}_i} \end{bmatrix} = \boldsymbol{E}_{EE_i}\cdot\boldsymbol{t}_{EE} + \boldsymbol{F}_{EE_i}\cdot\boldsymbol{M}_{1\_\boldsymbol{G}_i\boldsymbol{S}_i}\cdot\dot{\theta}_i \tag{21}$$

where $\boldsymbol{E}_{EE_i} = \begin{bmatrix} \boldsymbol{0}_6 \\ \boldsymbol{C}_{EE_i} \end{bmatrix}, \boldsymbol{F}_{EE_i} = \begin{bmatrix} \boldsymbol{E}_6 \\ \boldsymbol{D}_{EE_i} \end{bmatrix}$, $\boldsymbol{0}_6$ and $\boldsymbol{E}_6$ are the 6×6 zero matrix and identity matrix, respectively.

By virtue of Eqs. (20) and (21), the twist of the entire mechanism is

$$\boldsymbol{t} = \begin{bmatrix} \boldsymbol{t}_{C_1} \\ \vdots \\ \boldsymbol{t}_{C_6} \\ \boldsymbol{t}_{EE} \end{bmatrix} = \boldsymbol{E}_{EE_{1\_6}}\cdot\boldsymbol{t}_{EE} + \boldsymbol{F}_{EE_{1\_6}}\cdot\boldsymbol{T}_d\cdot\dot{\boldsymbol{\theta}} \tag{22}$$

where

$$\boldsymbol{E}_{EE_{1\_6}} = \begin{bmatrix} \boldsymbol{E}_{EE_1} \\ \vdots \\ \boldsymbol{E}_{EE_6} \\ \boldsymbol{E}_6 \end{bmatrix}, \quad \boldsymbol{F}_{EE_{1\_6}} = \begin{bmatrix} \boldsymbol{F}_{EE_1} & & \\ & \ddots & \\ & & \boldsymbol{F}_{EE_6} \\ & \boldsymbol{0}_{6\times36} & \end{bmatrix}$$

Substituting Eq. (20) into it produces

$$\boldsymbol{t} = \boldsymbol{T}_h\cdot\boldsymbol{T}_d\cdot\dot{\boldsymbol{\theta}} \tag{23}$$

where $\boldsymbol{T}_h = \boldsymbol{E}_{EE_{1\_6}}\cdot\boldsymbol{J}_{EE}^{-1}\cdot\boldsymbol{Q}_{\boldsymbol{GS}} + \boldsymbol{F}_{EE_{1\_6}}$. One can further obtain

$$\dot{\boldsymbol{t}} = \dot{\boldsymbol{T}}_h\cdot\boldsymbol{T}_d\cdot\dot{\boldsymbol{\theta}} + \boldsymbol{T}_h\cdot\boldsymbol{T}_d\cdot\ddot{\boldsymbol{\theta}} \tag{24}$$

If the mechanism under study is not redundantly actuated, its twist can be expressed by the independent active joint coordinates as those in (Rao, Saha, and Rao 2006) (Khan et al. 2005) (Khan et al. 2004). However, this is not the case in this RAPM, because the 6×1 vector $\dot{\boldsymbol{\theta}}$ is not independent, and from Eq. (8), one can find

$$\dot{\boldsymbol{\theta}} = \boldsymbol{J}_{\theta 1}\cdot\dot{\boldsymbol{q}}_{EE} \tag{25}$$

where $\boldsymbol{J}_{\theta 1} = \left[\boldsymbol{M}_{11(1,:)}^{T} \quad \cdots \quad \boldsymbol{M}_{16(1,:)}^{T}\right]^{T}$ is the 6×4 Jacobian matrix mapping $\dot{\boldsymbol{q}}_{EE}$ into $\dot{\boldsymbol{\theta}}$. Putting Eq. (25) into Eq. (23) yields

$$\boldsymbol{t} = \boldsymbol{T}\cdot\dot{\boldsymbol{q}}_{EE} \tag{26}$$

where $\boldsymbol{T} = \boldsymbol{T}_h\cdot\boldsymbol{T}_d\cdot\boldsymbol{J}_{\theta 1}$ is nothing but the NOC matrix which is decoupled into three matrices. In PMs without actuation redundancy as in (Rao, Saha, and Rao 2006) (Khan et al. 2005) (Khan et al. 2004), the NOC matrix is decoupled to two matrices. By contrast, in the RAPM, there are three decoupled matrices. From the symbolic computations above, they are full block, block diagonal, and full block, respectively.

The uncoupled dynamic model of the RAPM can be written in a compact form as

$$\boldsymbol{M}\cdot\dot{\boldsymbol{t}} + \boldsymbol{W}\cdot\boldsymbol{M}\cdot\boldsymbol{t} = \boldsymbol{w}^W + \boldsymbol{w}^C \tag{27}$$

where

$$\boldsymbol{M} = diag\left(\boldsymbol{M}_{\boldsymbol{G}_1\boldsymbol{S}_1} \quad \boldsymbol{M}_{\boldsymbol{S}_1\boldsymbol{M}_1} \quad \cdots \quad \boldsymbol{M}_{\boldsymbol{G}_6\boldsymbol{S}_6} \quad \boldsymbol{M}_{\boldsymbol{S}_6\boldsymbol{M}_6} \quad \boldsymbol{M}_{EE}\right)$$

$$\boldsymbol{W} = diag\left(\boldsymbol{W}_{\boldsymbol{G}_1\boldsymbol{S}_1} \quad \boldsymbol{W}_{\boldsymbol{S}_1\boldsymbol{M}_1} \quad \cdots \quad \boldsymbol{W}_{\boldsymbol{G}_6\boldsymbol{S}_6} \quad \boldsymbol{W}_{\boldsymbol{S}_6\boldsymbol{M}_6} \quad \boldsymbol{W}_{EE}\right)$$

$$\boldsymbol{w}^W = \begin{bmatrix} \boldsymbol{w}^W_{\boldsymbol{G}_1\boldsymbol{S}_1} \\ \boldsymbol{w}^W_{\boldsymbol{S}_1\boldsymbol{M}_1} \\ \vdots \\ \boldsymbol{w}^W_{\boldsymbol{G}_6\boldsymbol{S}_6} \\ \boldsymbol{w}^W_{\boldsymbol{S}_6\boldsymbol{M}_6} \\ \boldsymbol{w}^W_{EE} \end{bmatrix}, \quad \boldsymbol{w}^C = \begin{bmatrix} \boldsymbol{w}^C_{\boldsymbol{G}_1\boldsymbol{S}_1} \\ \boldsymbol{w}^C_{\boldsymbol{S}_1\boldsymbol{M}_1} \\ \vdots \\ \boldsymbol{w}^C_{\boldsymbol{G}_6\boldsymbol{S}_6} \\ \boldsymbol{w}^C_{\boldsymbol{S}_6\boldsymbol{M}_6} \\ \boldsymbol{w}^C_{EE} \end{bmatrix} \tag{28}$$

are the system mass matrix, the system angular velocity matrix, the system working wrench vector, and the system constraint wrench vector, respectively. Specifically,

$$\begin{aligned} \boldsymbol{M}_{\boldsymbol{G}_i\boldsymbol{S}_i} &= \mathrm{diag}\left(\boldsymbol{I}_{\boldsymbol{G}_i\boldsymbol{S}_i} \quad m_{\boldsymbol{G}_i\boldsymbol{S}_i}\cdot\boldsymbol{E}_3\right) \\ \boldsymbol{M}_{\boldsymbol{S}_i\boldsymbol{M}_i} &= \mathrm{diag}\left(\boldsymbol{I}_{\boldsymbol{S}_i\boldsymbol{M}_i} \quad m_{\boldsymbol{S}_i\boldsymbol{M}_i}\cdot\boldsymbol{E}_3\right) \\ \boldsymbol{M}_{EE} &= \mathrm{diag}\left(\boldsymbol{I}_{EE} \quad m_{EE}\cdot\boldsymbol{E}_3\right) \end{aligned} \tag{29}$$

are the 6×6 inertia dyad of the crank $\boldsymbol{G}_i\boldsymbol{S}_i$, the coupler $\boldsymbol{S}_i\boldsymbol{M}_i$, and the end effector, respectively, where $\boldsymbol{I}_{\boldsymbol{G}_i\boldsymbol{S}_i}, \boldsymbol{I}_{\boldsymbol{S}_i\boldsymbol{M}_i}, \boldsymbol{I}_{EE}$ are their inertia tensors in frame $\{S\}$, respectively, and $m_{\boldsymbol{G}_i\boldsymbol{S}_i}, m_{\boldsymbol{S}_i\boldsymbol{M}_i}, m_{EE}$ are their masses, respectively. In the system angular velocity matrix,

$$\begin{aligned} \boldsymbol{W}_{\boldsymbol{G}_i\boldsymbol{S}_i} &= \mathrm{diag}\left(\boldsymbol{\omega}_{\boldsymbol{G}_i\boldsymbol{S}_i}\times \quad \boldsymbol{0}_3\right), \\ \boldsymbol{W}_{\boldsymbol{S}_i\boldsymbol{M}_i} &= \mathrm{diag}\left(\boldsymbol{\omega}_{\boldsymbol{S}_i\boldsymbol{M}_i}\times \quad \boldsymbol{0}_3\right), \\ \boldsymbol{W}_{EE} &= \mathrm{diag}\left(\boldsymbol{\omega}_{EE}\times \quad \boldsymbol{0}_3\right) \end{aligned} \tag{30}$$

are the 6×6 angular velocity dyad of the crank $\boldsymbol{G}_i\boldsymbol{S}_i$, the coupler $\boldsymbol{S}_i\boldsymbol{M}_i$, and the end effector, respectively. In the system working wrench vector, as far as $\boldsymbol{G}_i\boldsymbol{S}_i$ is concerned, the external working wrench acting on it is

$$\boldsymbol{w}^W_{\boldsymbol{G}_i\boldsymbol{S}_i} = \boldsymbol{w}^A_{\boldsymbol{G}_i\boldsymbol{S}_i} + \boldsymbol{w}^G_{\boldsymbol{G}_i\boldsymbol{S}_i} \tag{31}$$

where $\boldsymbol{w}_{\boldsymbol{G}_i\boldsymbol{S}_i}^{A} = \boldsymbol{M}_{1\boldsymbol{G}_i\boldsymbol{S}_i} \cdot \tau_i$ and $\boldsymbol{w}_{\boldsymbol{G}_i\boldsymbol{S}_i}^{G} = \begin{bmatrix} \boldsymbol{0}_{3\times1} \\ -m_{\boldsymbol{G}_i\boldsymbol{S}_i} \cdot \boldsymbol{g} \end{bmatrix}$ are the wrenches from the actuator and the gravity, respectively. For the coupler $\boldsymbol{S}_i\boldsymbol{M}_i$, the external working wrench acting on it is only caused by its gravity, thus

$$\boldsymbol{w}_{\boldsymbol{S}_i\boldsymbol{M}_i}^{W} = \begin{bmatrix} \boldsymbol{0}_{3\times1} \\ -m_{\boldsymbol{S}_i\boldsymbol{M}_i} \cdot \boldsymbol{g} \end{bmatrix} \tag{32}$$

Concerning the end effector, its working wrench is

$$\boldsymbol{w}_{EE}^{W} = \boldsymbol{w}_{EE}^{G} + \boldsymbol{w}_{\boldsymbol{F}_B} \tag{33}$$

where $\boldsymbol{w}_{EE}^{G} = \begin{bmatrix} \boldsymbol{0}_{3\times1} \\ -m_{EE} \cdot \boldsymbol{g} \end{bmatrix}$ and $\boldsymbol{w}_{\boldsymbol{F}_B}$ are the wrenches from its gravity and the bite force, respectively.

In the system constraint wrench vector, $\boldsymbol{w}_{\boldsymbol{G}_i\boldsymbol{S}_i}^{C}$, $\boldsymbol{w}_{\boldsymbol{S}_i\boldsymbol{M}_i}^{C}$, and $\boldsymbol{w}_{EE}^{C}$ are the constraint wrenches acting at $\boldsymbol{G}_i\boldsymbol{S}_i$, $\boldsymbol{S}_i\boldsymbol{M}_i$, and the end effector, respectively. Specifically, $\boldsymbol{w}_{\boldsymbol{G}_i\boldsymbol{S}_i}^{C}$ is from the actuator and $\boldsymbol{S}_i\boldsymbol{M}_i$, $\boldsymbol{w}_{\boldsymbol{S}_i\boldsymbol{M}_i}^{C}$ is from $\boldsymbol{G}_i\boldsymbol{S}_i$ and the end effector, and $\boldsymbol{w}_{EE}^{C}$ is from the six couplers and the base at the two HKPs simultaneously.

Since the sole function of ideal constraint wrenches in a mechanism is to keep all bodies together, the sum of the power by them is zero

$$\boldsymbol{t}^T \cdot \boldsymbol{w}^C = \dot{\boldsymbol{q}}_{EE}^T \cdot \boldsymbol{T}^T \cdot \boldsymbol{w}^C = 0 \tag{34}$$

Because $\boldsymbol{q}_{EE}$ is the independent coordinate vector, $\dot{\boldsymbol{q}}_{EE}$ is free to vary, i.e.,

$$\boldsymbol{T}^T \cdot \boldsymbol{w}^C = 0 \tag{35}$$

From this step, the reason why the twist of the entire mechanism in Eq. (26) is expressed by $\dot{\boldsymbol{q}}_{EE}$ and the NOC is decomposed into three matrices can be discovered clearly.

After $\boldsymbol{T}^T$ is left-multiplied at each term of Eq. (27), the constraint wrench vector can be eliminated

$$\boldsymbol{T}^T \cdot \boldsymbol{M} \cdot \dot{\boldsymbol{t}} + \boldsymbol{T}^T \cdot \boldsymbol{W} \cdot \boldsymbol{M} \cdot \boldsymbol{t} = \boldsymbol{T}^T \cdot \boldsymbol{w}^W \tag{36}$$

Substituting Eqs. (23) and (24) into it generates

$$\begin{aligned} &\boldsymbol{J}_{\theta 1}^T \cdot \boldsymbol{\tau} \\ &= \boldsymbol{T}^T \cdot \left(\boldsymbol{M} \cdot \boldsymbol{T}_h \cdot \boldsymbol{T}_d \cdot \ddot{\boldsymbol{\theta}} + \left(\boldsymbol{M} + \boldsymbol{W} \cdot \boldsymbol{M} \right) \cdot \dot{\boldsymbol{T}}_h \cdot \boldsymbol{T}_d \cdot \dot{\boldsymbol{\theta}} \right) - \boldsymbol{J}_{\theta 1}^T \cdot \boldsymbol{\tau}_0 \end{aligned} \tag{37}$$

where

$$\boldsymbol{\tau}_0 = \boldsymbol{T}_d^T \cdot \left(\boldsymbol{J}_{EE}^{-1} \cdot \boldsymbol{Q}_{GS} \right)^T \cdot \left(\sum_{i=1}^{6} \boldsymbol{C}_{EE_i}^T \cdot \boldsymbol{w}_{\boldsymbol{S}_i\boldsymbol{M}_i}^W + \boldsymbol{w}_{EE}^W \right) + \boldsymbol{T}_d^T \cdot \begin{bmatrix} \boldsymbol{E}_{EE_1}^T \cdot \boldsymbol{w}_{\boldsymbol{S}_1\boldsymbol{M}_1}^W \\ \vdots \\ \boldsymbol{E}_{EE_6}^T \cdot \boldsymbol{w}_{\boldsymbol{S}_6\boldsymbol{M}_6}^W \end{bmatrix}$$

In Eq. (37), there are four equations and six unknowns, indicating the mechanism is redundantly actuated. The minimum-norm solution of the actuating torques is expressed as

$$\boldsymbol{\tau} = \left(\boldsymbol{J}_{\theta 1}^T \right)^+ \cdot \boldsymbol{R} \tag{38}$$

where $\left(\boldsymbol{J}_{\theta 1}^T \right)^+$ is the pseudo-inverse matrix of $\boldsymbol{J}_{\theta 1}^T$, and $\boldsymbol{R}$ is the right hand side of Eq. (37). Thereupon, the dynamic model of the RAPM has been built in the joint space.

NUMERICAL COMPUTATIONS AND DISCUSSIONS

Computational demands

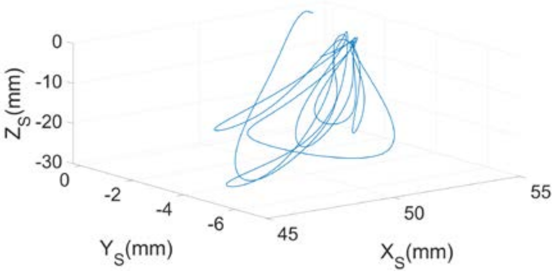

Fig. 2 A real incisor trajectory.

To verify the model, the mechanism is commanded to follow a real incisor trajectory by a healthy human subject which lasts 5 seconds shown in Figure. 2 in the 3D space. The corresponding mandibular motions in terms of the four elements of $\boldsymbol{q}_{EE}$ are computed, using the same method in Eq. (38) of (Cheng, Xu, and Shang 2015). The reacted bite force from the chewed foods is given in Figure. 3.

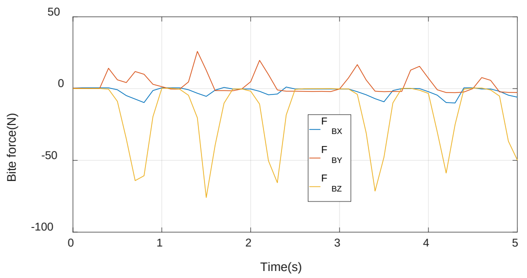

Fig. 3 3D bite force profiles on peanuts (Xu and Bronlund 2010).

The procedures are implemented in programs written in Matlab, using an Intel(R) Core(TM) i7-8700K CPU@3.70GHz and 32GB of RAM. The time consumption is 22.709s, and the actuating torques is given in the first subplot of Figure 4. Because the software at hand, i.e., Matlab is not able to compute redundant actuation mode, a software simulation cannot be performed to validate the numerical results. Thereby, the Lagrangian formulation is used as a second method to build the dynamics model, which is in the task space naturally. The torque differences from these two methods are presented in the second subplot of **Fig. 4**. The differences are very minor, proving the rightness of the built model.

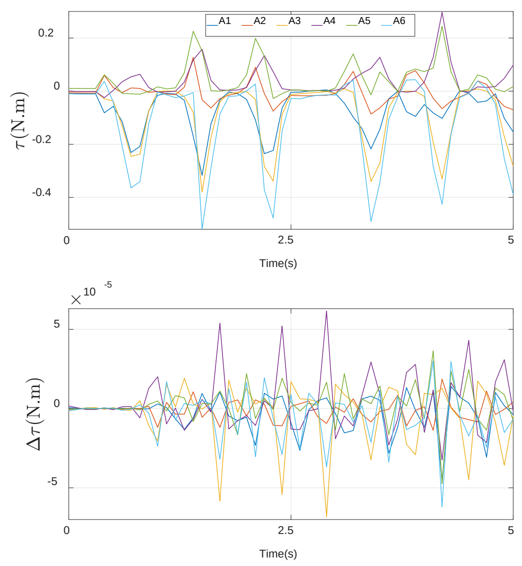

Fig. 4 Torques from the DeNOC and torque differences from two methods.

Influence of constraints at HKPs

It is remembered that the RAPM is generated by imposing two constraints at HKPs onto the end effector of the 6RSS PM. Thereby, the inverse dynamics of the 6RSS PM is also built by the DeNOC, as far as the role of these constraints in the dynamic model is concerned. In this circumstance, its inverse dynamics problem is reduced to solving a system of six linear algebraic equations in six unknowns. As can be found in PMs without actuation redundancy (Rao, Saha, and Rao 2006) (Khan et al. 2005), the NOC matrix is also decoupled into two matrices. The input torques can be uniquely determined and there is no pseudo-inverse computation as in the RAPM. The computational time in the 6RSS PM is 2.526s, which is only about 11.12% of that of the RAPM. As such, it indicates the HKPs considerably increase the computational complexity. The reason clearly roots in the complex expressions of parasitic motion variables Z and γ in Eq. (5), which greatly increase the computational demands. By contrast, in the 6RSS PM, Z and γ are directly used as DOFs which are much more straightforward.

The profiles of torques in the time history are similar to those in the first subplot of **Fig. 4** but with larger magnitudes. Thus, the actuating torques are not exhibited to save pages. To quantitatively justify and compare the influence by HKPs to the actuating torques, one index is set as

$$F = \frac{1}{N}\sum_{i=1}^{N}\|\boldsymbol{\tau}\|_i \tag{39}$$

where N is the number of sampling points in the time history, and $\|\boldsymbol{\tau}\|_i$ is the two-norm sum of the actuating torques at the ith time instant. The value of F is 0.1985N.m and 0.2727N.m in the RAPM and the 6RSS PM, respectively. The latter is as large as 1.37 times that of the former, indicating redundant actuation can minimise the input torques, which is a well-known opinion, even though redundant actuations in the mechanism are generated by converting two DOFs into parasitic motions under the constraints at HKPs. In other words, smaller torques are devoted to the remaining four DOFs and two parasitic motion variables.

Table 1 Comparison of the RAPM and the 6RSS PM

	RAPM	6RSS
Number of matrices decomposed from the NOC	3	2
Computational time (unit: s)	22.709	2.526
F (unit: N.m)	0.1985	0.2727

To better compare the RAPM and the 6RSS PM, their differences are summarised in Table 1.

CONCLUSION

The inverse dynamics in the joint space of a spatial RAPM constrained directly by the base at two HKPs was solved via the DeNOC. It is believed the first to apply this method to a RAPM constrained by the base directly. The scientific contributions in this paper are:

1. The model from the DeNOC is in the joint space, providing a great potential to facilitate the model-based control scheme in real-time.
2. The DeNOC in the RAPM is decoupled into three matrices, being very different from those in PMs without redundant actuations.
3. By comparing the RAPM and the 6RSS PM, the torques required by the parasitic motion variables in the RAPM are smaller than those by the corresponding DOFs in the 6RSS PM. Meanwhile, constraints at HKPs considerably raise the computational cost.

ACKNOWLEDGMENT

The authors sincerely appreciate the valuable time, suggestions, and comments from the editors and the reviewers.

REFERENCES

Bellakehal, S., Andreff, N., Mezouar, Y., Tadjine, M. 2011. "Force/position control of parallel robots using exteroceptive pose measurements." Meccanica 46 (1):195-205.

Cheng, C., Xu, W. L., Shang, J.Z.. 2015. "Kinematics, stiffness and natural frequency of a redundantly actuated masticatory robot constrained by two point-contact higher kinematic pairs." IEEE/RSJ International Conference on Intelligent Robots and Systems (IROS), Hamburg, Germany, Sept 28- Oct 2, 2015.

Cheng, H., Yiu, Y., Li, Z.X. 2003. "Dynamics and Control of Redundantly Actuated Parallel Manipulators." Mechatronics, IEEE/ASME Transactions on 8:483-491.

Clement, G., Schreiber, T. 2018. "Redundancy in Parallel Mechanisms: A Review." Applied Mechanics Reviews 70(1): 010802.

Huang, J., Chen, Y., Zhong, Z.H. 2013. "Udwadia-Kalaba Approach for Parallel Manipulator Dynamics." Journal of Dynamic Systems, Measurement, and Control 135 (6).

Jiang H.Z., Liu, Y.W. 2021. "Nonlinear analysis of compliant robotic fish locomotion." Journal of Vibration and Control 0 (0):1-13.

Khan, W., Krovi, V., Saha, S.K., Angeles, J.. 2004. "Recursive Kinematics and Inverse Dynamics for a Planar 3R Parallel Manipulator." Journal of Dynamic Systems, Measurement, and Control 127 (4):529-536.

Khan, W., Krovi, V., Saha, S.K., Angeles, J.. 2005. "Modular and Recursive Kinematics and Dynamics for Parallel Manipulators." Multibody System Dynamics 14 (3):419-455.

Liang, D., Song, Y.M., Sun, T., Dong, G. 2015. "Optimum design of a novel redundantly actuated parallel manipulator with multiple actuation modes for high kinematic and dynamic performance." Nonlinear Dynamics 83 (1):631-658.

Liu, X.F., Yao, J.T., Li, Q., Zhao, Y.S. 2022. "Coordination dynamics and model-based neural network synchronous controls for redundantly full-actuated parallel manipulator." Mechanism and Machine Theory 160:104284.

Merlet, J.P. 2012. Parallel robots. Vol. 74: Springer Science & Business Media.

Muller, A. 2005. "Internal Preload Control of Redundantly Actuated Parallel Manipulators-Its Application to Backlash Avoiding Control." IEEE Transactions on Robotics 21 (4):668-677.

Hanzaki, A.R., Saha, S.K., Rao, P.M. 2009. "An improved dynamic modeling of a multibody system with spherical joints." Multibody System Dynamics 21 (4):325-345.

Rao, K., Saha, S.K., Rao, P. 2006. "Dynamics Modelling of Hexaslides using the Decoupled Natural Orthogonal Complement Matrices." Multibody System Dynamics 15 (2):159-180.

Raoofian, A., Kamali, A., Taghvaeipour, A. 2017. "Forward dynamic analysis of parallel robots using modified decoupled natural orthogonal complement method." Mechanism and Machine Theory 115:197-217.

Saha, S.K. 1999. "Dynamics of Serial Multibody Systems Using the Decoupled Natural Orthogonal Complement Matrices." Journal of Applied Mechanics 66 (4):986-996.

Shang, W.W., Cong, S. 2014. "Robust nonlinear control of a planar 2-DOF parallel manipulator with redundant actuation." Robotics and Computer-Integrated Manufacturing 30 (6):597-604.

Wang, Y., Belzile, B., Angeles, J., Li, Q.C. 2019. "The Modeling of Redundantly Actuated Mechanical Systems." Journal of Mechanisms and Robotics 11 (6):061005.

Xu, W., Bronlund, J. 2010. Mastication Robots: Biological Inspiration to Implementation. Berlin, Germany: Springer-Verlag.

受兩個點接觸高副約束的冗余驅動並聯機構關節空間動力學逆解

程晨　袁曉靜　曾繁琦　羅偉蓬　張澤

西安技術學院機電一体化實驗室

摘要

本文提出了一個受到兩個點接觸高副約束的空間冗余驅動並聯機構的剛性動力學逆解。首先，完整地分析了它的受約束運動，之後，使用解耦自然正交分解法建立了關節空間的動力學模型，其非常適合於基於模型的運動控製。借助該模型，清晰地發現了高副約束在模型結構，計算時間，和驅動力矩上帶來的影響。自然正交矩陣分解為三個矩陣，這和非冗余驅動並聯機構非常不一樣。同時，通過對比該機構及其無高副約束的對比對象，發現高副約束極大增加了模型的計算時間。該機構的寄生運動所需力矩遠小於其對比對象相應的自由度所需驅動力矩。